NANO LETTERS

pubs.acs.org/NanoLett Letter

3D Ising Superconductivity in As-Grown Sn Intercalated $TaSe_2$ Crystal

Bo Zheng,[#] Xiaoming Zhang,[#] Kaipu Wang,[#] Ruimin Li,[#] Jin Cao, Changlong Wang, Haige Tan, Zhidong Li, Benchuan Lin, Peng Li, Chuanying Xi, Jingmin Zhang, Yalin Lu,[*] Wenguang Zhu, Zhongkai Liu, Shengyuan A. Yang, Lain-Jong Li, Feng Liu,[*] and Bin Xiang[*]

Cite This: *Nano Lett.* 2025, 25, 4895−4903 Read Online

ACCESS | Metrics & More | Article Recommendations | Supporting Information

ABSTRACT: 2D Ising superconductivity emerges in noncentrosymmetric 2D materials, differing from conventional 2D/3D superconductivity. Here, we report the synthesis of a new polymorph of intercalated layered materials, where two layers of Sn are intercalated in between every two layers of $TaSe_2$ (2Sn-2$TaSe_2$), in contrast to the commonly observed single-layer intercalation. Remarkably, the as-grown 2Sn-2$TaSe_2$ single crystals possess a high quality of crystallinity and showcase 3D Ising superconductivity. Transport measurements and theoretical calculations show that the 2Sn-2$TaSe_2$ having C_{3v} point group symmetry induces formation of Ising pairs, which intriguingly exhibits, on one hand, an in-plane upper critical field surpassing the Pauli limit by a factor of 2.6 like a 2D Ising superconductor but, on the other hand, a temperature- and field-dependent conductivity characteristic of conventional 3D superconductivity. Our findings demonstrate the persistent 2D Ising pairing in 3D, paving the way for exploring dimensional physical behaviors by intercalating layered materials.

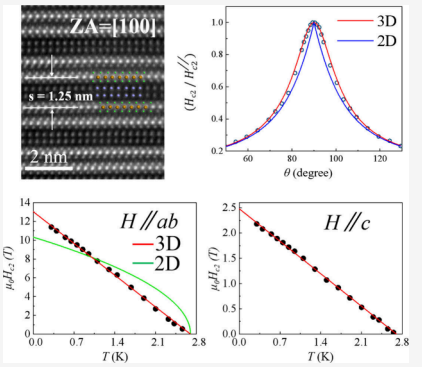

KEYWORDS: *bilayer intercalation, 3D Ising superconductivity, $SnTaSe_2$, noncentrosymmetry*

Two-dimensional (2D) materials are among the most popular materials being widely studied since the discovery of graphene,[1−4] as they exhibit many novel properties, such as 2D Ising superconductivity[5−7] discovered in 2D transition metal dichalcogenides (TMDs). Beyond the initial focus on single-layer 2D materials, much recent efforts have been made in multilayered materials that exhibit 2D characteristics, as exemplified by the twisted and intercalated layered materials.[4,8] Of our interest here, the intercalated layered materials of high crystallinity are formed by intercalating commonly a single layer of foreign atoms or molecules in-between the layers of host materials, such as the well-known intercalation of alkali atoms in graphite.[9] Remarkably, we have successfully synthesized a new polymorph of intercalated layered materials, where two layers of Sn are intercalated between every two layers of 2H-$TaSe_2$ (2Sn-2$TaSe_2$). The as-gown 2Sn-2$TaSe_2$ single crystals not only possess a high quality of crystallinity but also exhibit novel physical behavior of 3D Ising superconductivity.

The recent discovery of 2D Ising superconductivity is particularly intriguing because it defies the conventional wisdom of superconductivity by locking the spin of electrons to the crystal lattice, to enhance the robustness of superconductivity against external magnetic fields.[10,11] The Ising superconductivity is primarily observed in 2D TMDs that have a noncentrosymmetric structure and display strong spin−orbit coupling (SOC) to induce an Ising-like spin symmetry[5,12−21] locked with momentum. One approach to promote Ising pairing is by intercalating a 3D structure,[8,22,23] to reduce the interlayer interaction, so that 2D layers of Ising superconductors can be effectively "isolated" to locally break the inversion symmetry.

On the other hand, conventional 3D superconductivity occurs in bulk materials with isotropic pairing in all three spatial dimensions without spin-momentum locking. When 3D superconductors are confined to a single or few layers of thickness, they may retain the superconductivity in 2D with the same isotropic pairing mechanism as its 3D counterparts but a different pairing potential (or transition temperature),[24−26] behaving as conventional 2D superconductors[27,28] distinct from a 2D Ising superconductor. Therefore, an interesting question is whether there exists 3D Ising superconductivity, which preserves the 2D Ising pairing in an otherwise 3D superconductor.

In this article, we report the discovery of the 3D Ising superconductivity in the newly synthesized polymorph of 2Sn-

Received: January 9, 2025
Revised: March 11, 2025
Accepted: March 13, 2025
Published: March 17, 2025

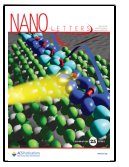

https://doi.org/10.1021/acs.nanolett.5c00196
Nano Lett. 2025, 25, 4895−4903

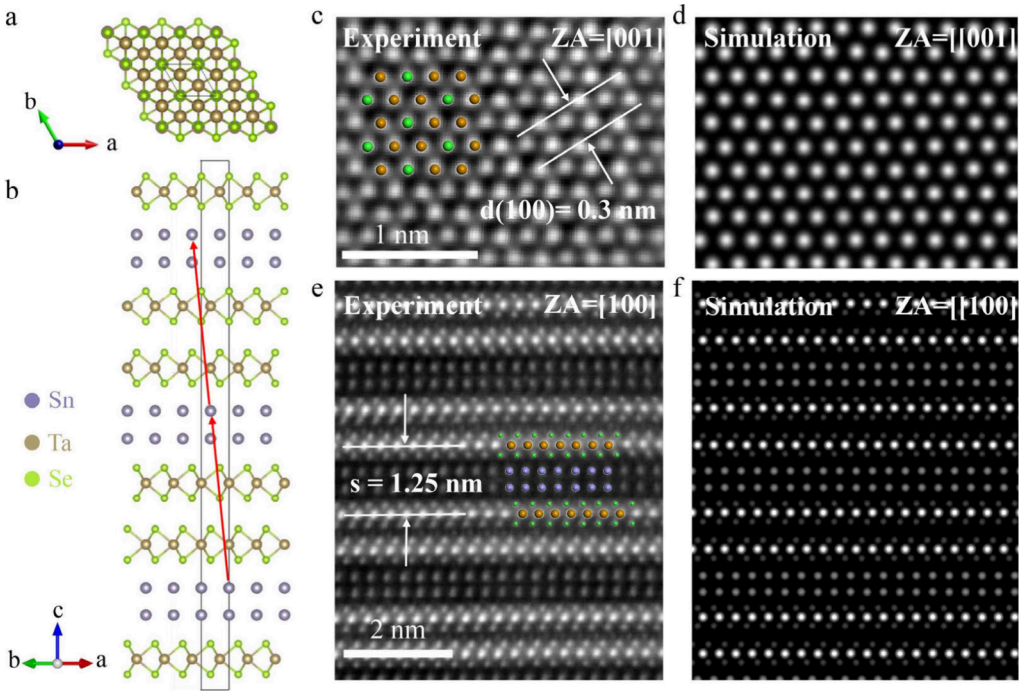

Figure 1. Crystal structure and morphologies of 2Sn-2$TaSe_2$. (a) Top view and (b) side view of the crystal structure of 2Sn-2$TaSe_2$. The purple, brown and green spheres represent Sn, Ta, and Se atoms, respectively. (c–f) HRSTEM image and the corresponding simulated HRSTEM images.

2$TaSe_2$ characterized with bilayer Sn intercalated bilayer $TaSe_2$, which is uniquely different from the commonly known layered materials with single layer intercalation, including single layer Sn intercalated single layer $TaSe_2$.[29,30] This intercalated of bilayer Sn results in the broken inversion symmetry in bulk 2Sn-2$TaSe_2$, which is distinct from the reported single-layer Sn intercalated bulk Sn-$TaSe_2$ with a central symmetry.[29] Through transport measurements and theoretical calculations, we reveal that the 2Sn-2$TaSe_2$ bulk crystal, having C_{3v} point group symmetry, facilitates the formation of Ising pairs in each $TaSe_2$ bilayer while at the same time exhibiting the transport characteristics of conventional 3D superconductivity. Remarkably, the *in-plane* upper critical field is measured to exceed the Pauli limit by a factor of 2.6, in agreement with our first-principles theoretical estimate, which is akin to the typical behavior of 2D Ising superconductors. Meantime, the 2Sn-2$TaSe_2$ crystal displays temperature- and field-dependent conductivity that follows the behavior of a 3D superconductor. Our findings suggest that 2D Ising pairing can persist in 3D systems, opening new avenues for exploring the intriguing interplay between 2D and 3D superconductivity and other dimensional physical behaviors by varying layer intercalation.

Figure 1a shows the new structure of 2Sn-2$TaSe_2$ of noncentrosymmetric symmetry with the space group of *R3m*, which is different from the reported centrosymmetric bulk $SnTaSe_2$ with a space group of $P6_3/mmc$.[29] The side view (Figure 1b) shows that two layers of $TaSe_2$ are sandwiched between two layers of Sn. We stress again that this unique structure is distinct from the other previously reported $SnTaSe_2$ structures (Supplementary Figure 1).[30,31] The new structure of 2Sn-2$TaSe_2$ was synthesized using a chemical vapor transport method (details in Experimental Section). The as-grown 2Sn-2$TaSe_2$ exhibits high crystallinity, as confirmed by the measurements of X-ray diffraction (XRD) (Supporting Information, Figure 2), transmission electron microscopy, and selected area electron diffraction (SAED) (Supporting Information, Figure 3). The representative XRD peaks are consistent with the identified space group *R3m* of 2Sn-2$TaSe_2$, showing noticeable differences from the reported data of $TaSe_2$ and $TaSe_3$ (Supplementary Figure 4). The in-plane and cross-sectional high-resolution scanning transmission electron microscopy (HRSTEM) images reveal a defect-free atomic structure of the as-grown 2Sn-2$TaSe_2$, in good agreement with the simulated results as shown in Figure 1c-f. The cross-sectional HRSTEM image also shows the stacking nature of Sn, Ta, and Se atoms, confirming that there are two layers of Sn atoms being inserted into the van der Waals gaps between the $TaSe_2$ bilayers. This leads to an increased inter-$TaSe_2$ bilayer spacing of 1.25 nm.

To reveal the chemical composition of the as-grown 2Sn-2$TaSe_2$, energy-dispersive X-ray spectroscopy (EDS) analysis was conducted. EDS mapping demonstrates a uniform distribution of elements Sn, Ta, and Se in the sample (Supplementary Figure 5). In addition, EDS spectra indicate that the molar ratio of the constituent elements Sn:Ta:Se is approximately 1:1:2 (Supplementary Figure 5). X-ray photoelectron spectroscopy (XPS) analysis was performed to further verify the sample's chemical composition and valence states (Supplementary Figure 6). Peaks at 485.5 and 493.9 eV can be attributed to Sn $3d_{5/2}$ and $3d_{3/2}$, respectively; peaks at 486.8 and 495.2 eV correspond to Sn^{4+} $3d_{5/2}$ and $3d_{3/2}$, respectively; peaks at 22.5/24.3 eV and 24.8/26.4 eV are associated with $4f_{7/2}/4f_{5/2}$ of Ta^{4+} and Ta^{5+}, respectively; and peaks at 53.1/54.1 eV and 53.8/54.8 eV are attributed to $3d_{5/2}/3d_{3/2}$ of Se^{2-} and Se^0, respectively. All these assignments are consistent with the previous reports,[32,33] establishing the elemental composition and corresponding valence states of as-grown 2Sn-2$TaSe_2$ single crystals.

To investigate the electronic structure, angle-resolved photoemission spectroscopy (ARPES) was measured at a temperature of 20 K. Figure 2a and Figure 2b show the stacks

https://doi.org/10.1021/acs.nanolett.5c00196
Nano Lett. 2025, 25, 4895−4903

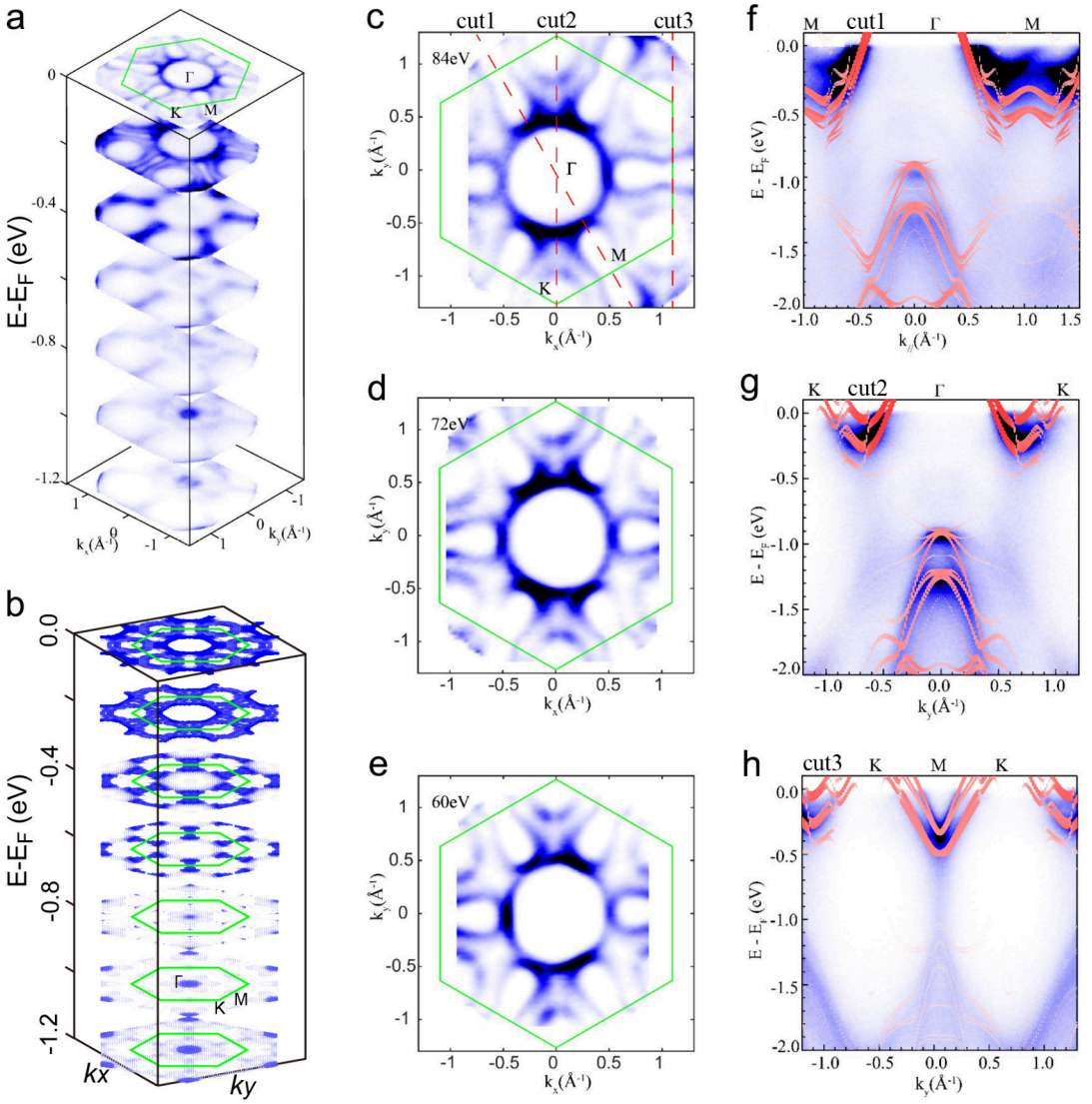

Figure 2. Electronic structure of 2Sn-2TaSe$_2$ measured with ARPES. (a, b) The constant energy surfaces sliced at every 0.2 eV. (c–e) The Fermion-surface measured with photon energy 84, 72, 60 eV, respectively. (f–h) The measured energy dispersions along the high-symmetry directions illustrated by the red dashed lines in (c). Part (b) and the red dotted lines within parts (f)–(h) are the theoretically calculated electronic structures contributed by the *d*-orbitals of Ta atoms.

of ARPES isoenergy surfaces of 2Sn-2TaSe$_2$, where one can see that there is a circle around the Γ/K point and a dog-bone-shaped feature at the M point. With the increasing binding energy, the circle around Γ points decreases and becomes a point at ∼1 eV while the circle around K point becomes larger. Figure 2c-e shows the Fermi surface measured with photon energies 84, 72, and 60 eV, respectively. The Fermi surfaces are almost identical at different photon energies, indicating the van der Waals layered nature of 2Sn-2TaSe$_2$. Figure 2f-h shows the measured energy band dispersions along the high-symmetry paths as marked by the red dashed lines in Figure 2c, which are in good agreement with the theoretical calculation results (the red lines in Figure 2f-h). Additionally, the calculations indicate that the electronic states around the Fermi level are mainly contributed by the *d*-orbitals of Ta atoms, with relatively small contribution from the *p*-orbitals of Sn and Se atoms (see Supplementary Figure 7).

The superconductivity of 2Sn-2TaSe$_2$ was investigated by electrical transport measurements. A sharp resistance-drop to zero is observed in the temperature dependence of the measured resistance (Figure 3a), showing a superconducting transition temperature T_c of 2.7 K, which is defined at the temperature where the resistance drops to 50% of the normal-state resistance.[34,35] To further verify the superconductivity, the temperature dependence of the magnetization under 10 Oe was measured in both zero-field-cooled (ZFC) and field-cooled (FC) modes, with the magnetic field applied parallel to the *c*-axis (Figure 3b). The emergence of a diamagnetic signal indicates that 2Sn-2TaSe$_2$ enters the superconducting state below 2.5 K, which is consistent with the resistance measurement. Furthermore, the $M(H)$ curve at 2 K (see inset of Figure 3b) exhibits a noticeable hysteresis, suggesting that 2Sn-2TaSe$_2$ is a type-II superconductor.[36,37]

To probe the dimensionality of bulk 2Sn-2TaSe$_2$ superconductivity, the current–voltage (I–V) curve was measured around the superconducting transition region. Figure 3c shows the I–V curve in the temperature range from 2.45 to 3.1 K on a log–log scale. Generally, for 2D superconductors, the I–V curve follows a power-law dependence ($V \propto I^{\alpha}$), based on the model of Berezinskii–Kosterlitz–Thouless (BKT) transi-

https://doi.org/10.1021/acs.nanolett.5c00196
Nano Lett. 2025, 25, 4895–4903

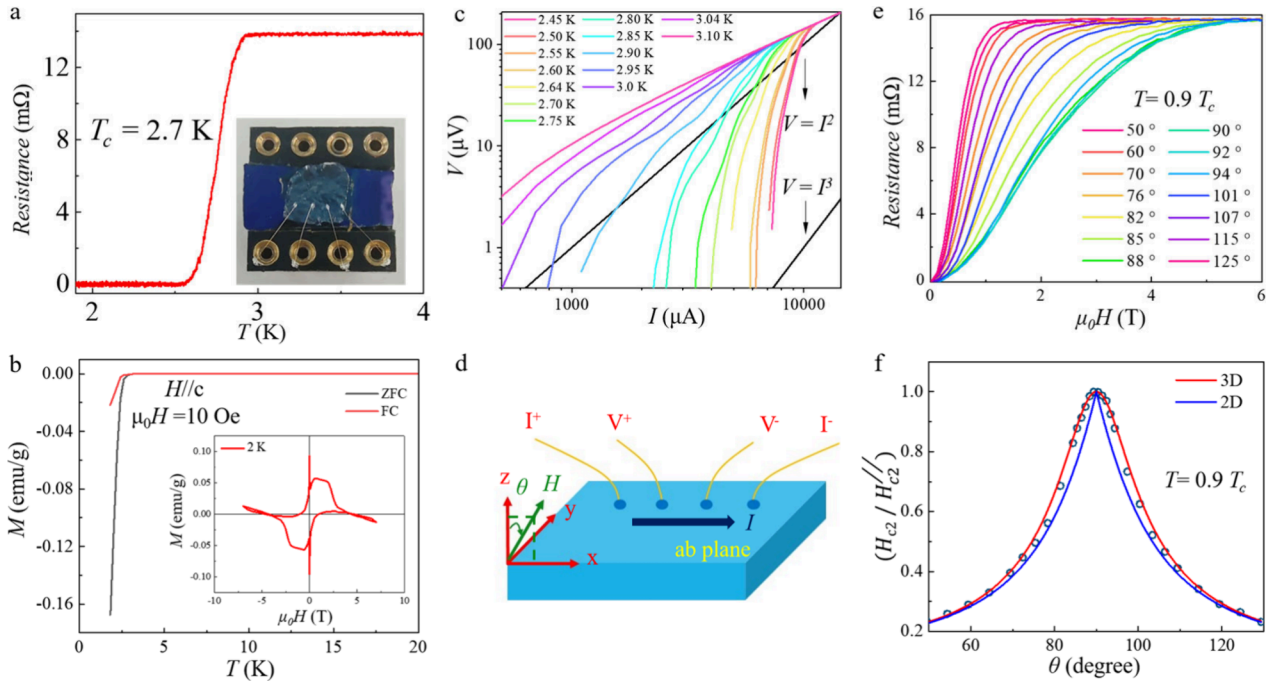

Figure 3. Characterization of superconducting properties of 2Sn-2$TaSe_2$. (a) Resistance as a function of temperature measured with current flowing in the *ab* plane, showing a superconducting transition at 2.7 K. The inset shows the optical image of the device. (b) The zero-field-cooling (ZFC) and field-cooling (FC) magnetic susceptibility curves measured with the external magnetic field μ_0H = 10 Oe applied along the *c* axis. The inset is magnetic field dependence of magnetization for $H\|c$ at T = 2 K. (c) The Voltage−current (V−I) relationship at different temperatures on a logarithmic scale. The long black line denotes $V = I^2$ and $V = I^3$. (d) The schematic diagram of the measurement setup, illustrating the orientation of the applied magnetic field. (e) The resistance of bulk 2Sn-$TaSe_2$ as a function of the magnetic field with different θ_{zx} at the temperature of T = 0.9T_c. (f) Angular dependence of the H_{c2} for 2Sn-$TaSe_2$. The black line and the red line were fitted by 2D Tinkham model $((H_{c2}(\theta)|\cos\theta|/H_{c2}^{\perp} + (H_{C2}(\theta)\sin\theta/H_{c2}^{\|})^2 = 1)$ and 3D GL anisotropic mass model $((H_{c2}(\theta)\cos\theta/H_{c2}^{\perp} + (H_{C2}(\theta)\sin\theta/H_{c2}^{\|})^2 = 1)$, respectively.

tion.[38−40] However, our measured data on a log−log scale exhibits obviously a nonlinear dependence. This indicates that the superconducting behavior of bulk 2Sn-2$TaSe_2$ should not be considered as 2D superconductivity.

Next, the angular dependence of the upper critical field $H_{c2}(\theta)$ was studied. A schematic diagram of the testing device is shown in Figure 3d, where θ_{zx} is defined as the angle between the direction of the magnetic field and the *c*-axis. At T = 0.9T_c, the resistance as a function of the magnetic field under different field rotation angles θ_{zx} is plotted in Figure 3e. It can be seen that for $\theta_{zx} < 90°$, H_{c2} increases with the increase of θ_{zx} and reaches the maximum when $\theta_{zx} = 90°$. For $\theta_{zx} > 90°$, H_{c2} shows an opposite trend, which decreases with the increase of θ_{zx}. Figure 3f shows the angular dependence of $H_{c2}(\theta)$ normalized by the *in-plane* $H_{c2}^{\|}$. For 3D and 2D superconductors, the angular dependence of $H_{c2}(\theta)$ can be fit by anisotropic mass 3D Ginsburg-Landau (GL) model, $[Hc2(\theta)\text{-}\cos\theta/H_{c2}^{\perp})^2 + (H_{c2}(\theta/H_{c2}^{\|})^2$ and 2D Tinkham model, $[(H_{c2}(\theta)|\cos\theta|/H_{c2}^{\perp} + (H_{c2}(\theta/H_{c2}^{\|})^2 = 1]$, respectively.[38,39,41−43] Here, the extracted in-plane $H_{c2}^{\|}$ of Figure 3f is defined as the 50% of resistance in the R-H curve from Figure 3e. Typically, the curve of $H_{c2}(\theta)$ takes the shape of a bell for the 3D GL model, while it takes the shape of a cusp for the 2D Tinkham model. The blue and red lines in Figure 3f were fit by the 2D Tinkham and 3D GL model, respectively. Clearly, one sees that $H_{c2}(\theta)$ is well described by the 3D GL model only, indicating again that 2Sn-2$TaSe_2$ exhibits 3D superconductivity.

Figure 4a and 4b shows the magnetic field dependence of resistance at different temperatures when the field is applied parallel to the *ab*-plane ($H\|ab$) and *c*-plane ($H\|c$), respectively. The superconductivity is gradually suppressed with an increasing magnetic field for both $H\|ab$ and $H\|c$. In addition, the superconducting transition moves to lower magnetic field with the increasing temperature. The temperature dependences of the in-plane and out-of-plane upper critical fields $H_{c2}^{\|}(T)$ and $H_{c2}^{\perp}(T)$ are plotted in Figure 4c and 4d, respectively. H_{c2} is evaluated using the standard of the 50% normal-state resistance on the $R(H)$ curve. The red and green solid lines in Figure 4c represent the fitting curves by the 3D and 2D GL model,[35,44] respectively. One finds that the temperature dependence of $H_{c2}^{\|}(T)$ can be well fitted by 3D but not 2D GL theory. The upper critical field of $H_{c2}^{\|}(0)$ = 13.04 T and of $H_{c2}^{\perp}(0)$ = 2.48 T can be extrapolated from the linear relationship between H_{c2} and T, leading to an aspect ratio of $\gamma = H_{c2}^{\|}(0)/H_{c2}^{\perp}(0)$ = 5.25. In addition, the corresponding zero-temperature coherence length is calculated to be, respectively, $\xi_{\|}(0)$ = 11.52 nm and $\xi_{\perp}(0)$ = 2.19 nm. These results show a highly anisotropic superconducting behavior in 3D. In particular, one notices that the vertical coherence length $\xi_{\perp}(0)$ (2.19 nm) is larger than the inter-$TaSe_2$ bilayer spacing (1.25 nm), rendering the 3D nature of the 2Sn-2$TaSe_2$ superconductivity, which may arise from the Josephson tunneling or proximity effect. In addition, based on the microscopic Klemm−Luther−Beasley (KLB) theory,[45−47] a dimensionality parameter $r = \frac{4}{\pi}\left(\frac{\xi^{\perp}(0)}{s/2}\right)^2$, can be used to characterize the dimensionality of a superconductor, for which $r < 1$ signals a transition from 3D to 2D behavior. When $r \to 0$, $H_{c2}^{\|}(T)$ shows a $(T_c - T)^{1/2}$ scaling, while for large r, $H_{c2}^{\|}(T)$ shows a $(T_c - T)$ linear scaling. For our as-grown 2Sn-2$TaSe_2$ crystals, the parameter r is calculated to be ∼ 15.6 (Supplementary Note 1), suggesting it falls well into the 3D

https://doi.org/10.1021/acs.nanolett.5c00196
Nano Lett. 2025, 25, 4895−4903

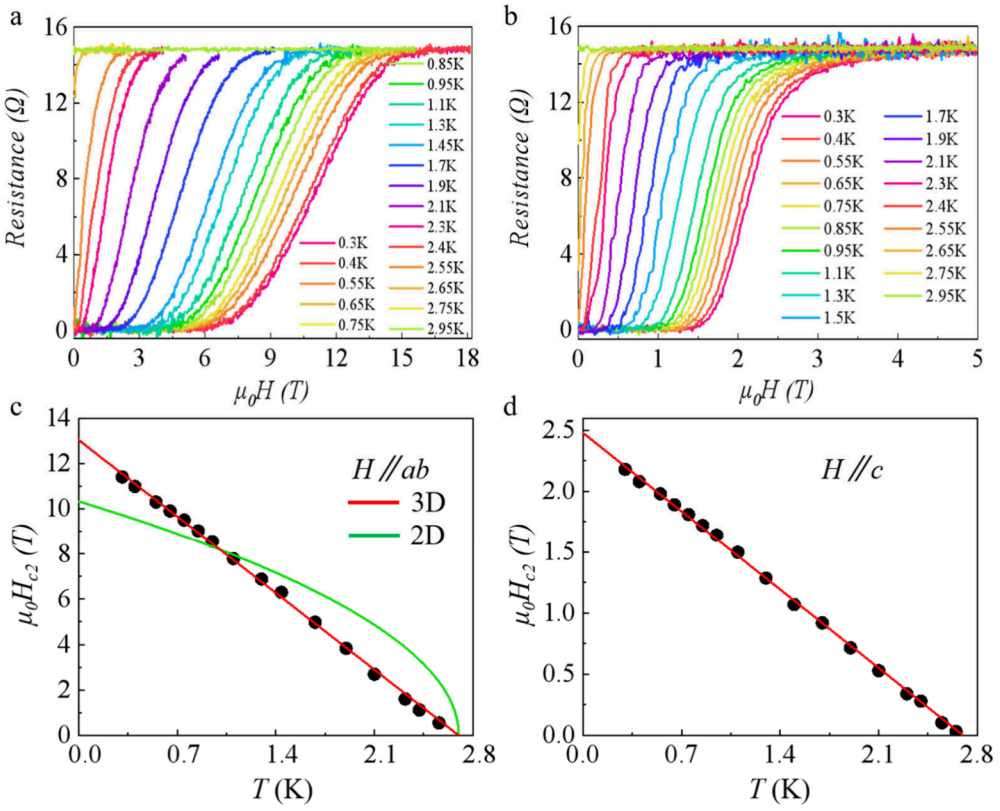

Figure 4. Electrical transport behavior and magnetic response of 2Sn-2TaSe$_2$. The Magnetic field dependence of the resistance for (a) $H\|ab$ and (b) $H\|c$ at various temperatures. The critical field H_{c2} as a function of temperature T for (c) $H\|ab$ and (d) $H\|c$ (fitting curves shown in red and green lines using the 3D and 2D GL models, respectively).

regime. Our results show that bulk 2Sn-2TaSe$_2$ with two layers of atoms intercalated in every two layers of host material exhibits a 3D superconducting behavior not a 2D superconducting behavior as reported in the bulk TMDs.[5−7] It is interesting to note that the resulting 3D Ising superconductor is prone to exfoliation into 2D materials (Supplementary Figure 8).

Despite the 3D superconductivity as evidenced above, remarkably, the *in-plane* upper critical field $H_{c2}^{\|}(0)$ exceeds the Pauli paramagnetic field ($H_p \approx 1.84T_c$)[5,6,22,41] by a significant ratio of $H_{c2}^{\|}(0)/H_p = 2.62$. Generally, various mechanisms might be responsible for enhancing the in-plane upper critical field at low temperature, such as dimensional crossover,[38] multiband effects,[48,49] and spin−orbit scattering.[45,49] However, none of these is found to be applicable to 2Sn-2TaSe$_2$ (Supplementary Note 2). Instead, we attribute the underlying microscopic mechanism for the enhancement of in-plane upper critical field to the spin-momentum locking[20,38,50] property induced by intrinsic SOC effect. The crystal structure of as-grown 2Sn-2TaSe$_2$ has C_{3v} point group symmetry. The presence of inversion symmetry breaking and large SOC strength leads to an effective magnetic field perpendicular to the TaSe$_2$ bilayer near K and K′ points, while the field direction near the Γ point tends to lie in the plane of TaSe$_2$ bilayer. This makes electron states on the Fermi surface contours surrounding K and K′ points possess out-of-plane spin polarization, while those on the Fermi surface contours surrounding the Γ point have spins polarized to the in-plane directions, which are schematically plotted in Figure 5a.

The Fermi-surface spin texture and hence the effective local magnetic fields are confirmed by first-principles calculations

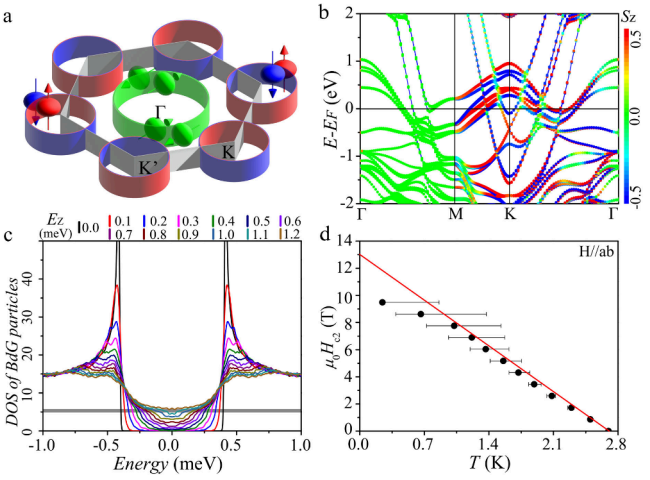

Figure 5. Calculated electronic and superconducting properties of 2Sn-2TaSe$_2$. (a) The schematic diagram of Fermi surface with in-plane directed spin polarization for the electronic states surrounding Γ point and out-of-plane spin polarized states surrounding K and K′ points. (b) Band structures of 2Sn-2TaSe$_2$ with the spin expectation values of S_z being marked by colored dots. (c) The simulated DOS of BdG particles under different in-plane Zeeman energy E_Z. The gray horizontal region is employed to determine the magnitudes of superconducting gaps under different Zeeman fields. (d) The dependence of in-plane upper critical fields on temperatures summarized from figure (c), where the red line represents the experimental measurement.

(see method), as shown by the calculated electronic band structures superimposed with spin expectation values in Figure

https://doi.org/10.1021/acs.nanolett.5c00196
Nano Lett. 2025, 25, 4895−4903

5b (see also Supplementary Figure 9). The out-of-plane spin polarization lifts the Kramers degeneracy at K and K′ points to enable Ising superconductivity within the $TaSe_2$ bilayer.[19,51] The in-plane upper critical field of each $TaSe_2$ bilayer alone should be comparable with that of single layer TaS_2,[19] and the lower critical field of 2Sn-2$TaSe_2$ is likely due to the existence of Fermi surface contours surrounding the Γ point with in-plane spin polarization, which come from the *p* orbitals of intercalating Sn layers (Supplementary Figure 7). This intriguing picture is confirmed by simulating the density-of-state (DOS) of Bogoliubov-de-Gennes (BdG) particles under different Zeeman energy E_Z by diagonalizing a first-principles BdG Hamiltonian H_{BdG} (see Computational Methods).[52] In Figure 5c, one can clearly see that the superconducting gaps are gradually suppressed by an applied in-plane Zeeman field. Furthermore, assuming the superconducting gaps correspond to the values of the DOS of BdG particles equaling half of the normal-state DOS, the dependence of in-plane upper critical fields on temperature was obtained, as shown in Figure 5d, which agrees well with the experimental results.

In summary, we have demonstrated 3D Ising superconductivity in a stable new polymorph of the bilayer Sn intercalated bilayer $TaSe_2$. It arises from the van der Waals stacking of 2D Ising superconductor of $TaSe_2$ bilayers mediated with Sn bilayers, where the Ising spin texture of individual $TaSe_2$ layer is largely preserved on the Fermi surface around the corners of the Brillouin zone (K and K'), while 3D superconducting states emerges at the zone center (Γ) from the *p*-orbitals of intercalating Sn bilayers. Consequently, it presents a form of highly anisotropic 3D superconductivity and, most strikingly, a unique form of 3D Ising superconductivity that exhibits an *in-plane* upper critical magnetic field exceeding the Pauli paramagnetic limit field by a factor of 2.6, comparable to 2D Isling superconductors. Our findings shed new lights on understanding the role of dimensionality and symmetry, as well as layer intercalation in superconductivity, and provide a novel material platform for exploring the intriguing interplay between 2D and 3D, and between Ising and non-Ising superconductivity.

Note: During the preparation of this manuscript, we become aware of a recent related work on 3D Ising superconductivity in a different heterostructure of $4H_b$-TaS_2.[53]

EXPERIMENTAL SECTION

Single-Crystal Growth. The air-stable 2Sn-2$TaSe_2$ single crystals were grown via a chemical vapor transport method. High-purity powders of Sn, Ta, and Se were mixed in a molar ratio of 1:1:2 and thoroughly ground to ensure homogeneity. The resulting mixture was sealed together with a small amount of iodine and $SnBr_2$ in a vacuum-sealed quartz tube, with iodine and $SnBr_2$ serving as the transport agent. Subsequently, the sealed quartz tube was placed in a double-temperature-zone tubular furnace. The high-temperature zone and low-temperature zone were heated at a rate of 1 °C/min to 700 and 600 °C, respectively, and maintained at these temperatures for 2 days. The temperature was then raised to 1050−950 °C and held at 1050/950 °C for 7 days. Shiny crystals (see the inset of Figure 3a) were obtained after the furnace was cooled to room temperature.

Characterization of Bulk Crystals. The phase purity of the samples was detected by using X-ray diffraction with Cu Kα. Electrical transport measurements were conducted using a physical properties measurement system (Quantum Design, PPMS-9 T). The electrical transport measurements under high magnetic fields were performed at the High Magnetic Field Laboratory in Hefei, China, using standard AC lock-in techniques and a water-cooled magnet (∼30 T). The magnetic properties were measured by using a superconducting quantum interference magnetometer (SQUID, Quantum Design).

Transfer of Nanosheets. The 2Sn-2$TaSe_2$ nanosheets were obtained by mechanical exfoliation using Scotch tape. The exfoliated nanosheets were directly transferred onto Cu grids using a dry transfer method in a glovebox. First, PDMS was applied onto precleaned glass slides, and then the nanosheets exfoliated by Scotch tape were transferred onto the PDMS. The glass slide with PDMS was then secured onto a transfer stage, and the selected 2Sn-2$TaSe_2$ nanosheets were brought into contact with preprepared Cu grids. Subsequently, the glass slide was slowly lifted, leaving the nanosheets adhered to the Cu grids for subsequent high-angle annular dark-field scanning transmission electron microscopy (HAADF-STEM) imaging. Similarly, the exfoliated 2Sn-2$TaSe_2$ nanosheets were transferred to a prepatterned Ti/Au (8 nm/25 nm) Hall Bar through the dry transfer method.

Computational Methods. The Vienna *ab initio* simulation pack (VASP) was used to perform first-principles calculations on electronic property of 2Sn-$TaSe_2$ based on density functional theory (DFT).[54,55] The Perdew−Burke−Ernzerhof generalized gradient approximation[56] and the projector augmented wave pseudopotential[57] were employed with the energy cutoff of 500 eV. The lattice constants of 2Sn-2$TaSe_2$ were set to experiment values with the interlayer spacing between $TaSe_2$ bilayers fixed at 1.25 nm. Self-consistent calculations were performed with considering the SOC effect, and the Brillouin zone was sampled by the uniform 12 × 12 × 1 **k**-point mesh, which enables us to plot the constant energy surfaces. The self-consistent CHGCAR file was employed to calculate electronic band structures along high-symmetry directions by performing nonself-consistent calculations, where the orbital contributions of each element and spin expectation values were extracted from the PROCAR file.

ARPES Methods. ARPES measurements were performed at the 03U beamlines of Shanghai Synchrotron Radiation Facilities (SSRF). The measured sample temperature was below 30 K and the vacuum level was better than 5.0×10^{-11} Torr in all setups. The angle resolution was 0.2°, and the overall energy resolution was better than 10 meV/5 meV for 100 eV/20 eV photons, respectively. The sample was cleaved in-suit.

ASSOCIATED CONTENT

Supporting Information

The Supporting Information is available free of charge at https://pubs.acs.org/doi/10.1021/acs.nanolett.5c00196.

Crystal structures, additional characterization data, estimation of parameters and related graphics, and comparative study on the superconducting properties of common TMDs and 2Sn-2$TaSe_2$ (PDF)

AUTHOR INFORMATION

Corresponding Authors

Bin Xiang − *Department of Materials Science & Engineering, Hefei National Research Center for Physical Sciences at the Microscale, CAS Key Lab of Materials for Energy Conversion, Anhui Laboratory of Advanced Photon Science and*

https://doi.org/10.1021/acs.nanolett.5c00196
Nano Lett. 2025, 25, 4895−4903

Technology, University of Science and Technology of China, Hefei 230026, China; Hefei National Laboratory, University of Science and Technology of China, Heifei 230088, China; orcid.org/0000-0001-8254-8640; Email: binxiang@ustc.edu.cn

Yalin Lu − *Department of Materials Science & Engineering, Hefei National Research Center for Physical Sciences at the Microscale, CAS Key Lab of Materials for Energy Conversion, Anhui Laboratory of Advanced Photon Science and Technology, University of Science and Technology of China, Hefei 230026, China; Hefei National Laboratory, University of Science and Technology of China, Heifei 230088, China;* Email: yllu@ustc.edu.cn

Feng Liu − *Department of Materials Science and Engineering, University of Utah, Salt Lake City, Utah 84112, United States;* orcid.org/0000-0002-3701-8058; Email: fliu@eng.utah.edu

Authors

Bo Zheng − *Department of Materials Science & Engineering, Hefei National Research Center for Physical Sciences at the Microscale, CAS Key Lab of Materials for Energy Conversion, Anhui Laboratory of Advanced Photon Science and Technology, University of Science and Technology of China, Hefei 230026, China;* orcid.org/0000-0001-9703-6365

Xiaoming Zhang − *College of Physics and Optoelectronic Engineering, Ocean University of China, Qingdao, Shandong 266100, China;* orcid.org/0000-0003-0756-9526

Kaipu Wang − *School of Physical Science and Technology, ShanghaiTech University, 201210 Shanghai, China*

Ruimin Li − *Department of Materials Science & Engineering, Hefei National Research Center for Physical Sciences at the Microscale, CAS Key Lab of Materials for Energy Conversion, Anhui Laboratory of Advanced Photon Science and Technology, University of Science and Technology of China, Hefei 230026, China;* orcid.org/0009-0005-7709-7773

Jin Cao − *Research Laboratory for Quantum Materials, IAPME, University of Macau, Macau, China*

Changlong Wang − *Department of Materials Science & Engineering, Hefei National Research Center for Physical Sciences at the Microscale, CAS Key Lab of Materials for Energy Conversion, Anhui Laboratory of Advanced Photon Science and Technology, University of Science and Technology of China, Hefei 230026, China;* orcid.org/0000-0002-4663-7221

Haige Tan − *Department of Materials Science & Engineering, Hefei National Research Center for Physical Sciences at the Microscale, CAS Key Lab of Materials for Energy Conversion, Anhui Laboratory of Advanced Photon Science and Technology, University of Science and Technology of China, Hefei 230026, China*

Zhidong Li − *School of Microelectronics, University of Science and Technology of China, Hefei 230052, China;* orcid.org/0009-0008-8574-5621

Benchuan Lin − *Shenzhen Institute for Quantum Science and Engineering, Southern University of Science and Technology, Shenzhen 518055, China*

Peng Li − *School of Microelectronics, University of Science and Technology of China, Hefei 230052, China*

Chuanying Xi − *Anhui Province Key Laboratory of Condensed Matter Physics at Extreme Conditions, High Magnetic Field Laboratory, Chinese Academy of Sciences, Hefei 230031, China*

Jingmin Zhang − *Electron Microscopy Laboratory, School of Physics, Peking University, Beijing 100871, China*

Wenguang Zhu − *Hefei National Laboratory, University of Science and Technology of China, Heifei 230088, China; International Center for Quantum Design of Functional Materials (ICQD), Department of Physics, University of Science and Technology of China, Hefei, Anhui 230026, China;* orcid.org/0000-0003-0819-595X

Zhongkai Liu − *School of Physical Science and Technology, ShanghaiTech University, 201210 Shanghai, China;* orcid.org/0000-0003-3373-8039

Shengyuan A. Yang − *Research Laboratory for Quantum Materials, IAPME, University of Macau, Macau, China*

Lain-Jong Li − *Department of Mechanical Engineering and Department of Physics, The University of Hong Kong, Hong Kong 999077, China;* orcid.org/0000-0002-4059-7783

Complete contact information is available at: https://pubs.acs.org/10.1021/acs.nanolett.5c00196

Author Contributions

#(B.Z., X.Z., K.W., and R.L.) These authors contributed equally to this work

Notes

The authors declare no competing financial interest.

■ ACKNOWLEDGMENTS

The authors thank Prof. Zhenyu Zhang, Prof. Zhenyu Wang, and Dr. Xukun Feng for valuable discussions. This work was supported by the NSFC (52373309; 12004357; 92365204; 12274298; 51627901), Innovation Program for Quantum Science and Technology (2021ZD0302801), and the National Key R&D program of China (No. 2022YFA1604400/03; No. 2023YFA1610100). F.L. acknowledges the financial support from DOE-BES (No. DE-FG02-04ER46148). This research was partially carried out at the Instruments Center for Physical Sciences, the USTC Center for Micro and Nanoscale Research and Fabrication.

■ REFERENCES

(1) Novoselov, K. S.; Geim, A. K.; Morozov, S. V.; Jiang, D.; Katsnelson, M. I.; Grigorieva, I. V.; Dubonos, S. V.; Firsov, A. A. Two-dimensional gas of massless Dirac fermions in graphene. *Nature* **2005**, *438* (7065), 197−200.

(2) Zhang, Y.; Tan, Y.-W.; Stormer, H. L.; Kim, P. Experimental observation of the quantum Hall effect and Berry's phase in graphene. *Nature* **2005**, *438* (7065), 201−204.

(3) Si, C.; Sun, Z.; Liu, F. Strain engineering of graphene: a review. *Nanoscale* **2016**, *8* (6), 3207−3217.

(4) González, J.; Stauber, T. Ising superconductivity induced from spin-selective valley symmetry breaking in twisted trilayer graphene. *Nat. Commun.* **2023**, *14* (1), 2746.

(5) Lu, J.; Zheliuk, O.; Leermakers, I.; Yuan, N. F.; Zeitler, U.; Law, K. T.; Ye, J. Evidence for two-dimensional Ising superconductivity in gated MoS_2. *Science* **2015**, *350* (6266), 1353−1357.

(6) Xi, X.; Wang, Z.; Zhao, W.; Park, J.-H.; Law, K. T.; Berger, H.; Forró, L.; Shan, J.; Mak, K. F. Ising pairing in superconducting $NbSe_2$ atomic layers. *Nat. Phys.* **2016**, *12* (2), 139−143.

(7) Cui, J.; Li, P.; Zhou, J.; He, W.-Y.; Huang, X.; Yi, J.; Fan, J.; Ji, Z.; Jing, X.; Qu, F.; et al. Transport evidence of asymmetric spin-orbit coupling in few-layer superconducting $1T_d$-$MoTe_2$. *Nat. Commun.* **2019**, *10* (1), 2044.

(8) Trahms, M.; Grosse, C.; Alemayehu, M. B.; Hite, O. K.; Chiatti, O.; Mogilatenko, A.; Johnson, D. C.; Fischer, S. F. Superconductive

coupling in tailored $[(SnSe)_{1+\delta}]_m(NbSe_2)_1$ multilayers. *Supercond. Sci. Technol.* **2018**, *31* (6), 065006.
(9) Zhang, W.; Yan, J.; Chen, C.-H.; Lei, L.; Kuo, J.-L.; Shen, Z.; Li, L.-J. Molecular adsorption induces the transformation of rhombohedral-to Bernal-stacking order in trilayer graphene. *Nat. Commun.* **2013**, *4* (1), 2074.
(10) Polski, R. M. *Electronic Correlations and Topology in Graphene Moiré Multilayers and InAs/GaSb-Derivative Systems*; California Institute of Technology, 2023.
(11) Falson, J.; Xu, Y.; Liao, M.; Zang, Y.; Zhu, K.; Wang, C.; Zhang, Z.; Liu, H.; Duan, W.; He, K.; et al. Type-II Ising pairing in few-layer stanene. *Science* **2020**, *367* (6485), 1454−1457.
(12) Lu, J.; Zheliuk, O.; Chen, Q.; Leermakers, I.; Hussey, N. E.; Zeitler, U.; Ye, J. Full superconducting dome of strong Ising protection in gated monolayer WS_2. *Natl. Acad. Sci. USA* **2018**, *115* (14), 3551−3556.
(13) Wickramaratne, D.; Khmelevskyi, S.; Agterberg, D. F.; Mazin, I. Ising superconductivity and magnetism in $NbSe_2$. *Phys. Rev. X* **2020**, *10* (4), 041003.
(14) Zhou, B. T.; Yuan, N. F.; Jiang, H.-L.; Law, K. T. Ising superconductivity and Majorana fermions in transition-metal dichalcogenides. *Phys. Rev. B* **2016**, *93* (18), 180501.
(15) Liu, Y.; Xu, Y.; Sun, J.; Liu, C.; Liu, Y.; Wang, C.; Zhang, Z.; Gu, K.; Tang, Y.; Ding, C.; et al. Type-II Ising superconductivity and anomalous metallic state in macro-size ambient-stable ultrathin crystalline films. *Nano Lett.* **2020**, *20* (8), 5728−5734.
(16) Li, W.; Huang, J.; Li, X.; Zhao, S.; Lu, J.; Han, Z. V.; Wang, H. Recent progresses in two-dimensional Ising superconductivity. *Mater. Today. Phys.* **2021**, *21*, 100504.
(17) Wan, P.; Zheliuk, O.; Yuan, N. F.; Peng, X.; Zhang, L.; Liang, M.; Zeitler, U.; Wiedmann, S.; Hussey, N. E.; Palstra, T. T.; et al. Orbital Fulde-Ferrell-Larkin-Ovchinnikov state in an Ising superconductor. *Nature* **2023**, *619* (7968), 46−51.
(18) Devarakonda, A.; Inoue, H.; Fang, S.; Ozsoy-Keskinbora, C.; Suzuki, T.; Kriener, M.; Fu, L.; Kaxiras, E.; Bell, D. C.; Checkelsky, J. G. Clean 2D superconductivity in a bulk van der Waals superlattice. *Science* **2020**, *370* (6513), 231−236.
(19) De la Barrera, S. C.; Sinko, M. R.; Gopalan, D. P.; Sivadas, N.; Seyler, K. L.; Watanabe, K.; Taniguchi, T.; Tsen, A. W.; Xu, X.; Xiao, D.; et al. Tuning Ising superconductivity with layer and spin-orbit coupling in two-dimensional transition-metal dichalcogenides. *Nat. Commun.* **2018**, *9* (1), 1427.
(20) Xing, Y.; Zhao, K.; Shan, P.; Zheng, F.; Zhang, Y.; Fu, H.; Liu, Y.; Tian, M.; Xi, C.; Liu, H.; et al. Ising superconductivity and quantum phase transition in macro-size monolayer $NbSe_2$. *Nano Lett.* **2017**, *17* (11), 6802−6807.
(21) Zeng, J.; Liu, E.; Fu, Y.; Chen, Z.; Pan, C.; Wang, C.; Wang, M.; Wang, Y.; Xu, K.; Cai, S.; et al. Gate-induced interfacial superconductivity in 1T-$SnSe_2$. *Nano Lett.* **2018**, *18* (2), 1410−1415.
(22) Zhang, H.; Rousuli, A.; Zhang, K.; Luo, L.; Guo, C.; Cong, X.; Lin, Z.; Bao, C.; Zhang, H.; Xu, S.; et al. Tailored Ising superconductivity in intercalated bulk $NbSe_2$. *Nat. Phys.* **2022**, *18* (12), 1425−1430.
(23) Chiatti, O.; Mihov, K.; Griffin, T. U.; Grosse, C.; Alemayehu, M. B.; Hite, K.; Hamann, D.; Mogilatenko, A.; Johnson, D. C.; Fischer, S. F. Tuning metal/superconductor to insulator/superconductor coupling via control of proximity enhancement between $NbSe_2$ monolayers. *J. Phys-Condens. Mater.* **2023**, *35* (21), 215701.
(24) Hsu, J.; Kapitulnik, A. Superconducting transition, fluctuation, and vortex motion in a two-dimensional single-crystal Nb film. *Phys. Rev. B* **1992**, *45* (9), 4819.
(25) Guo, Y.; Zhang, Y.-F.; Bao, X.-Y.; Han, T.-Z.; Tang, Z.; Zhang, L.-X.; Zhu, W.-G.; Wang, E.; Niu, Q.; Qiu, Z.; et al. Superconductivity modulated by quantum size effects. *Science* **2004**, *306* (5703), 1915−1917.
(26) Saito, Y.; Nojima, T.; Iwasa, Y.; et al. Highly crystalline 2D superconductors. *Nat. Rev. Mater.* **2017**, *2* (1), 16094.
(27) Si, C.; Liu, Z.; Duan, W.; Liu, F. First-Principles Calculations on the Effect of Doping and Biaxial Tensile Strain on Electron-Phonon Coupling in Graphene. *Phys. Rev. Lett.* **2013**, *111* (19), 196802.
(28) Zhang, X.; Zhou, Y.; Cui, B.; Zhao, M.; Liu, F. Theoretical discovery of a superconducting two-dimensional metal-organic framework. *Nano Lett.* **2017**, *17* (10), 6166−6170.
(29) Eppinga, R.; Wiegers, G. A generalized scheme for niobium and tantalum dichalcogenides intercalated with post-transition elements. *Physica B+C* **1980**, *99* (1−4), 121−127.
(30) Adam, M. L.; Liu, Z.; Moses, O. A.; Wu, X.; Song, L. Superconducting properties and topological nodal lines features in centrosymmetric $Sn_{0.5}TaSe_2$. *Nano. Res.* **2021**, *14*, 2613−2619.
(31) Gentile, P.; Driscoll, D.; Hockman, A. Preparation and Mössbauer effect of tin intercalates of layered transition metal dichalcogenides. *Inorg. Chim. Acta* **1979**, 35, 249−253.
(32) Li, P.; Fu, W.; Zhuang, P.; Cao, Y.; Tang, C.; Watson, A. B.; Dong, P.; Shen, J.; Ye, M. Amorphous Sn/crystalline SnS_2 nanosheets via in situ electrochemical reduction methodology for highly efficient ambient N_2 fixation. *Small* **2019**, *15* (40), 1902535.
(33) Wang, H.; Chen, Y.; Zhu, C.; Wang, X.; Zhang, H.; Tsang, S. H.; Li, H.; Lin, J.; Yu, T.; Liu, Z.; et al. Synthesis of Atomically Thin 1T-$TaSe_2$ with a Strongly Enhanced Charge-Density-Wave Order. *Adv. Funct. Mater.* **2020**, *30* (34), 2001903.
(34) Li, Y.; Wu, Z.; Zhou, J.; Bu, K.; Xu, C.; Qiao, L.; Li, M.; Bai, H.; Ma, J.; Tao, Q.; et al. Enhanced anisotropic superconductivity in the topological nodal-line semimetal In_xTaS_2. *Phys. Rev. B* **2020**, *102* (22), 224503.
(35) Wang, H.; Huang, X.; Lin, J.; Cui, J.; Chen, Y.; Zhu, C.; Liu, F.; Zeng, Q.; Zhou, J.; Yu, P.; et al. High-quality monolayer superconductor $NbSe_2$ grown by chemical vapour deposition. *Nat. Commun.* **2017**, *8* (1), 394.
(36) Chen, D.-Y.; Wu, Y.; Jin, L.; Li, Y.; Wang, X.; Duan, J.; Han, J.; Li, X.; Long, Y.-Z.; Zhang, X.; et al. Superconducting properties in a candidate topological nodal line semimetal $SnTaS_2$ with a centrosymmetric crystal structure. *Phys. Rev. B* **2019**, *100* (6), 064516.
(37) Yang, X.; Yu, T.; Xu, C.; Wang, J.; Hu, W.; Xu, Z.; Wang, T.; Zhang, C.; Ren, Z.; Xu, Z.-a.; et al. Anisotropic superconductivity in the topological crystalline metal $Pb_{1/3}TaS_2$ with multiple Dirac fermions. *Phys. Rev. B* **2021**, *104* (3), 035157.
(38) Anderson, P. W. Theory of dirty superconductors. *J. Phys. Chem. Solids.* **1959**, *11* (1−2), 26−30.
(39) Xu, C.; Wang, L.; Liu, Z.; Chen, L.; Guo, J.; Kang, N.; Ma, X.-L.; Cheng, H.-M.; Ren, W. Large-area high-quality 2D ultrathin Mo_2C superconducting crystals. *Nat. Mater.* **2015**, *14* (11), 1135−1141.
(40) He, Q. L.; Liu, H.; He, M.; Lai, Y. H.; He, H.; Wang, G.; Law, K. T.; Lortz, R.; Wang, J.; Sou, I. K. Two-dimensional superconductivity at the interface of a Bi_2Te_3/FeTe heterostructure. *Nat. Commun.* **2014**, *5* (1), 4247.
(41) Wan, P.; Zheliuk, O.; Yuan, N. F.; Peng, X.; Zhang, L.; Liang, M.; Zeitler, U.; Wiedmann, S.; Hussey, N. E.; Palstra, T. T.; et al. Orbital Fulde-Ferrell-Larkin-Ovchinnikov state in an Ising superconductor. *Nature* **2023**, *619* (7968), 46−51.
(42) Tinkham, M. Effect of fluxoid quantization on transitions of superconducting films. *Phys. Rev.* **1963**, *129* (6), 2413.
(43) Baidya, P.; Sahani, D.; Kundu, H. K.; Kaur, S.; Tiwari, P.; Bagwe, V.; Jesudasan, J.; Narayan, A.; Raychaudhuri, P.; Bid, A. Transition from three-to two-dimensional Ising superconductivity in few-layer $NbSe_2$ by proximity effect from van der Waals heterostacking. *Phys. Rev. B* **2021**, *104* (17), 174510.
(44) Wawro, A. Superconductivity in Ni/Pb modulated films. *J. Low Temp. Phys.* **1994**, *94*, 351−359.
(45) Klemm, R. A.; Luther, A.; Beasley, M. Theory of the upper critical field in layered superconductors. *Phys. Rev. B* **1975**, *12* (3), 877.
(46) Coleman, R.; Eiserman, G.; Hillenius, S.; Mitchell, A.; Vicent, J. Dimensional crossover in the superconducting intercalated layer compound 2H-TaS_2. *Phys. Rev. B* **1983**, *27* (1), 125.
(47) Klemm, R. A.; Beasley, M.; Luther, A. The upper critical field of layered superconductors. *J. Low Temp. Phys.* **1974**, *16*, 607−613.

https://doi.org/10.1021/acs.nanolett.5c00196
Nano Lett. 2025, 25, 4895−4903

(48) Gurevich, A. Enhancement of the upper critical field by nonmagnetic impurities in dirty two-gap superconductors. *Phys. Rev. B* **2003**, *67* (18), 184515.
(49) Yang, H.; Zhou, Y.; Li, L.; Chen, Z.; Zhang, Z.; Wang, S.; Wang, J.; Chen, X.; An, C.; Zhou, Y.; et al. Pressure-induced superconductivity in quasi-one-dimensional semimetal Ta_2PdSe_6. *Phys. Rev. Mater.* **2022**, *6* (8), 084803.
(50) Saito, Y.; Nakamura, Y.; Bahramy, M. S.; Kohama, Y.; Ye, J.; Kasahara, Y.; Nakagawa, Y.; Onga, M.; Tokunaga, M.; Nojima, T.; et al. Superconductivity protected by spin-valley locking in ion-gated MoS_2. *Nat. Phys.* **2016**, *12* (2), 144−149.
(51) Xing, Y.; Yang, P.; Ge, J.; Yan, J.; Luo, J.; Ji, H.; Yang, Z.; Li, Y.; Wang, Z.; Liu, Y.; et al. Extrinsic and intrinsic anomalous metallic states in transition metal dichalcogenide Ising superconductors. *Nano Lett.* **2021**, *21* (18), 7486−7494.
(52) Zhang, X.; Jin, K.-H.; Mao, J.; Zhao, M.; Liu, Z.; Liu, F.; et al. Prediction of intrinsic topological superconductivity in Mn-doped GeTe monolayer from first-principles. *npj Comput. Mater.* **2021**, *7* (1), 44.
(53) Yang, F.; Zhang, H.; Mandal, S.; Meng, F.; Fabbris, G.; Said, A.; Lozano, P. M.; Rajapitamahuni, A.; Vescovo, E.; Nelson, C. Signature of Orbital Driven Finite Momentum Pairing in a 3D Ising Superconductor. *arXiv*, 2407.10352 [cond-mat.supr-con], 2024; https://arxiv.org/abs/2407.10352, submission date:14 Jul 2024 (accessed 2024-07-29).
(54) Hohenberg, P.; Kohn, W. Inhomogeneous electron gas. *Phys. Rev.* **1964**, *136* (3B), B864.
(55) Kohn, W.; Sham, L. J. Self-consistent equations including exchange and correlation effects. *Phys. Rev.* **1965**, *140* (4A), A1133.
(56) Perdew, J. P.; Burke, K.; Ernzerhof, M. Generalized gradient approximation made simple. *Phys. Rev. Lett.* **1996**, *77* (18), 3865.
(57) Blöchl, P. E. Projector augmented-wave method. *Phys. Rev. B* **1994**, *50* (24), 17953.

https://doi.org/10.1021/acs.nanolett.5c00196
Nano Lett. 2025, 25, 4895−4903